A Novel NIR–Red Spectral Domain Evapotranspiration Model From the Chinese GF-1 Satellite: Application to the Huailai Agricultural Region of China

Yunjun Yao, Shunlin Liang, *Fellow, IEEE,* Joshua B. Fisher, Yuhu Zhang, Jie Cheng, *Senior Member, IEEE*, Jiquan Chen, Kun Jia, Xiaotong Zhang, Xiangyi Bei, Ke Shang, Xiaozheng Guo, and Junming Yang

Abstract—The Chinese GF-1 satellite, the first satellite of the China High-resolution Earth Observation System launched in 2013, can be used to help estimate evapotranspiration (LE), which is important for myriad hydroclimatic and ecosystem science and applications. We propose a novel approach to use the GF-1 visible and near-infrared (VNIR) measurements at 16 m and 4-day resolutions to estimate LE. The NIR (near-infrared)–red spectral-domain (NRSD) model is coupled to a perpendicular soil moisture index (PSI) and a perpendicular vegetation index (PVI). We applied the model to the Huailai agricultural region of China with 55 scenes of GF-1 imagery during 2013–2017 and validated using ground measurements with footprint models for two eddy-covariance (EC) flux tower sites and one large aperture scintillometer (LAS) site. The results illustrate that the terrestrial daily LE can be estimated with squared correlation coefficients (R^2) of 0.77–0.84 ($p < 0.01$) and root-mean-square error (RMSE) values of 17.9–21.5 W/m^2 among all three sites. The site-calibrated statistics are improved by 0.14–0.25 for R^2 and decreased by 4.2–8.3 W/m^2 for RMSE as compared to the commonly used universal PT-JPL model. A satisfactory performance is achieved across all experimental conditions, encouraging the application of the NRSD model to estimate LE for other broad regions.

Index Terms—Chinese GF-1, Evapotranspiration, NIR–red spectral space, perpendicular soil moisture index (PSI), perpendicular vegetation index (PVI).

I. Introduction

EVAPOTRANSPIRATION (LE), i.e., the total water loss from surface soil evaporation, vegetation transpiration, and vegetation interception evaporation, plays a crucial role in agricultural drought detection, crop yield forecasting, water resource management, and climate change research [1]–[7]. In much of the temperate semiarid regions of Northern China (e.g., the Huailai agricultural region), water deficiency is placing major constraints on crop production and economic development [8], [9]. There is, therefore, a need to quantify water availability by estimating terrestrial LE. While conventional detailed ground-based observations [e.g., Lysimeter, energy balance Bowen ratio (BR), and eddy-covariance (EC) observations] can accurately measure LE at the local scale from a few meters to hundreds of meters [10]–[16], a limited number of *in situ* measurements, their representations of the landscape, and associated high costs prevent us from having spatially and temporally continuous spectra LE at the landscape and regional scales that are needed for timely and location-specific management of ecosystems.

Remote sensing is the most feasible means to estimate terrestrial LE across large regions by retrieving terrestrial biophysical variables that affect LE, including land surface temperature (LST), albedo, soil moisture (SM), land cover types, leaf area index (LAI), and vegetation index (VI, e.g., normalized difference VI and NDVI) [17]–[22]. Especially, the Chinese GF-1 satellite, the first satellite of the Major National Science and Technology Project of China, has provided high spatial resolution (16 m) remotely sensed data with wide coverage (800 km) and high revisit frequency (4 days) for estimating land surface biophysical variables on regional scale [23]. However, very few literature works have reported

Yunjun Yao, Jie Cheng, Kun Jia, Xiaotong Zhang, Xiangyi Bei, Ke Shang, Xiaozheng Guo, and Junming Yang are with the State Key Laboratory of Remote Sensing Science, Faculty of Geographical Science, Beijing Normal University, Beijing 100875, China (e-mail: boyyunjun@163.com; brucechan2003@126.com; jiakun@bnu.edu.cn; xtngzhang@bnu.edu.cn; xiang yibei@mail.bnu.edu.cn; shangke@mail.bnu.edu.cn; boyxiaozheng@mail.bnu.edu.cn; julming@163.com).

Shunlin Liang is with the Department of Geographical Sciences, University of Maryland, College Park, MD 20742 USA (e-mail: sliang@umd.edu).

Joshua B. Fisher is with the Joint Institute for Regional Earth System Science and Engineering, University of California at Los Angeles, Los Angeles, CA 90095-7228 USA (e-mail: joshbfisher@gmail.com).

Yuhu Zhang is with the College of Resource Environment and Tourism, Capital Normal University, Beijing 100048, China (e-mail: zhang_yuhu@163.com).

Jiquan Chen is with the Department of Geography, Environment, and Spatial Sciences, Michigan State University, East Lansing, MI 48823 USA (e-mail: jqchen@msu.edu).

Color versions of one or more of the figures in this article are available online at https://ieeexplore.ieee.org.

Digital Object Identifier 10.1109/TGRS.2020.3020125

the real-time LE models with good robustness to estimate LE using Chinese GF-1 data. Therefore, the development of the land surface LE methods from Chinese GF-1 data is urgently required.

Currently, satellite-based approaches for terrestrial LE estimations fall into two categories: thermal LST-based methods [19], [24]–[26] and optical VI-based methods [27]–[30]. The former includes surface energy balance (SEB)-based one- and two-source models [17], [20], [31]–[33] and spatial context-texture information-based LST-VI triangular or trapezoidal methods [34]–[36]. The overviews of these methods have been provided since the 1990s [19], [37]–[39]. Although thermal LST-based methods can easily capture water stress information without requiring soil hydraulic property and precipitation data, they are difficult to apply for the operational estimations of large heterogeneous regions due to the coarser spatial resolution as compared to visible and near-infrared (VNIR) data and infrequent availability of undisturbed thermal infrared images [40], [41]. Moreover, some satellite data of high spatial resolutions lack thermal observations such as data generated by the Chinese GF-1, a high spatial resolution satellite with four spectral bands in the optical domain, but no thermal band.

Optical VI-based methods rely on satellite-derived densities of green vegetation, with varying sensitivities [42]. Compared to the thermal LST-based methods, VI-based methods can estimate terrestrial LE at higher spatial resolutions from short-wave satellite, with a time sampling frequency of VI being a less concern, because VIs change insignificantly compared with LST in several days [43]–[45]. More importantly, several previous studies have reported that optical VI-based methods perform better at LE estimation than thermal LST-based methods [46], [47]. For instance, Cleugh *et al.* [48] compared LST-based SEB models to VI-based methods from the Moderate Resolution Imaging Spectroradiometer (MODIS) data and concluded that VI-based methods adequately estimate LE in Australia, whereas LST-based SEB models fail due to large errors in sensible heat flux (H) estimations propagated from small errors in LST. Similarly, Glenn *et al.* [46] compared satellite-based methods (LST-, mid-infrared-, and VI-based methods) and found that VIs provide the better estimations of LE than thermal bands [root mean square error (RMSE) of 18.5 W/m^2 for the VI-based method versus 24.7 W/m^2 for the LST-based method]. The Ecosystem Spaceborne Thermal Radiometer Experiment on Space Station (ECOSTRESS) employs a combination of high-resolution LST measured on the International Space Station with high-resolution VI from Landsat and Sentinel to produce operational LE at 70 m [49].

However, VIs do not account for SM impacts on the soil evaporation (LE$_s$) and cannot detect soil evaporation rate changes under severe water stress. Fortunately, spatially distributed crop coefficient (K_c) values calculated from precipitation (P) and irrigation data from soil water balance models have been widely applied to estimate LE$_s$ for agricultural water resource assessment [50]. Subsequently, several auxiliary methods based on meteorological variables [diurnal air temperature range (DTaR), relative humidity (RH), and vapor pressure deficit (VPD)] and microwave-derived SM products have been successfully used to parameterize SM contributions

in LE$_s$ estimation [6], [18], [29], [45], [51], [52]. However, these methods cannot estimate LEs at high spatial resolutions due to sparse meteorological observations and coarse-resolution microwave SM products.

Fortunately, several NIR (near-infrared)–red spectral space methods have been developed based on the reflective and absorptive features of canopy and bare soils in the NIR and red spectral domain (NRSD) to characterize the spatial variability of high-resolution SM for monitoring surface dryness conditions [53]–[56]. For example, Ghulam *et al.* [54] proposed a perpendicular drought index (PDI) based on the spatial characteristics of moisture distribution in NIR–red space from Landsat data and found that the PDI is highly correlated with ground-measured 0–20 cm mean SM values with the correlation coefficients of $R^2 = 0.49$ ($p < 0.01$). The distance drought index (DDI) [57] and triangle soil moisture index (TSMI) [58] were also successfully derived from the NIR–red triangular space for SM and drought monitoring. In principle, high-resolution LE$_s$ can be estimated from SM variability in the NIR and red spectral spaces of Chinese GF-1 data, and the NIR–red spectral space method may perform better than methods based on meteorological variables and coarse-resolution microwave SM products. However, there is a lack of similar studies on estimating high-resolution terrestrial LE using the NIR–red spectral space method and Chinese GF-1 data.

Here, we propose an NRSD model by integrating the perpendicular soil moisture index (PSI) and the VI (PVI) from Chinese GF-1 data to calculate the Priestley–Taylor (PT) coefficient for estimating daily terrestrial LE. We have two main objectives. First, we evaluate the proposed NRSD model using ground measurements with the footprint models for EC flux tower sites (EC1 and EC2) and one large aperture scintillometer (LAS) site in the Huailai agricultural region of China for 2013–2017. Second, we apply the NRSD model to the Huailai agricultural region to map daily LE.

II. Theoretical Background and Model Logic

Since the proposed model for estimating the PT coefficient is based on the NIR and red bands of Chinese GF-1 data, a brief introduction to this NIR–red spectral space is provided in Section II-A. Then, NIR–red-based vegetation and SM indices and an NRSD model for LE estimation are described in Sections II-B and II-C, respectively. Finally, the comparisons to another PT model, PT-JPL [18], are provided in Section II-D.

A. NIR–Red Spectral Space

The presented scatter plot of the atmospheric corrected NIR, red reflectance spectrum from a Chinese GF-1 image containing different land cover types shows a typical triangular shape (Fig. 1). The position of a pixel in the triangle is determined by several environmental factors, including SM, soil properties, and vegetation types and cover. As SM and vegetation cover are the two main factors that determine the position of a random pixel in the NIR–red spectral space, different surface dryness conditions and vegetation types have a specific regular
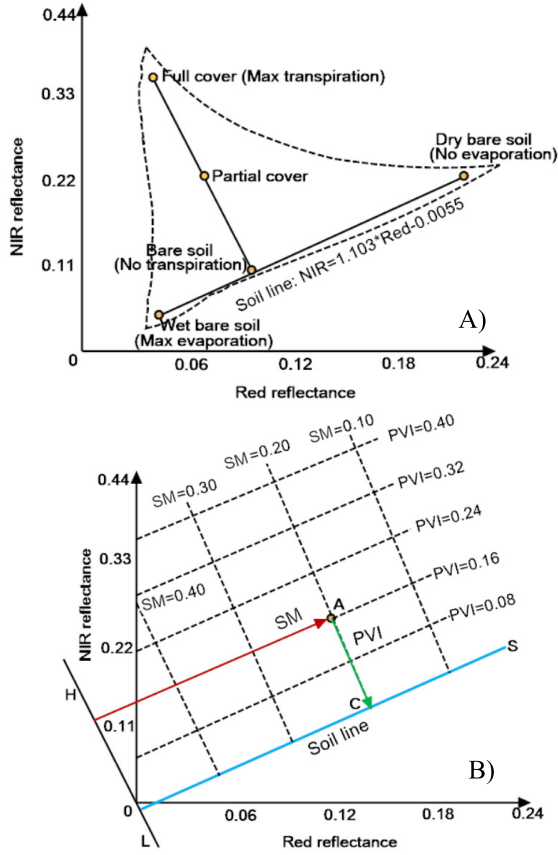
Fig. 1. (a) NIR–red spectral space from Chinese GF-1 data. (b) Definitions of the soil line and PVI (revised after [53], [55]).

Fig. 2. Definition of the PSI (revised after [55]).

distribution in this spectral space [53]. Here, pixels with high NIR reflectance and low red values are distributed in the upper vertex of the triangle (Fig. 1), i.e., highest levels of vegetation coverage and vegetation transpiration. As surface vegetation varies from full cover (maximum transpiration) and partial cover (partial transpiration) to bare soil (no transpiration) in a given pixel, its positioning moves toward the soil line that connects wet bare soil to dry bare soil. Therefore, pixels with equal vegetation fractional cover (F_c) values yield isolines parallel to the soil line in the NIR–red spectral space.

The soil line characterizes the spectral behavior of nonvegetated pixels, with its varying surface SM considerably [54], [55]. Pixels with the same SM values are positioned along the isolines and are perpendicular to the soil line [58], [59]. As the surface SM increases, isolines move from the upper right of the NIR–red spectral space to the lower left. In other words, the distance between the coordinate origin and any pixel in the NIR–red spectral space represents the severity of surface water stress. The farther this distance is, the greater the degree of surface water stress and the less SM there will be. However, these concepts associated with the soil line and upper regions of the triangle present uncertainties resulted from the complexities of soil properties and vegetation cover in the NIR–red spectral space [53], [58].

B. NIR–Red-Based Vegetation and Soil Moisture Indices

1) Perpendicular Vegetation Index: The PVI is an index for vegetation growth conditions by calculating the distance from
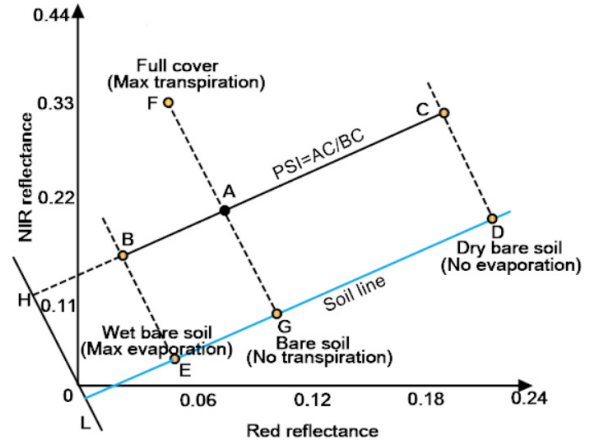
isolines to the soil line toward the upper vertex in the NIR–red spectral space (Fig. 1) [59]

$$\text{PVI} = \frac{\rho_{\text{nir}} - k\rho_{\text{red}} - b}{\sqrt{1 + k^2}} \quad (1)$$

where ρ_{nir} and ρ_{red} refer to the reflectance of the NIR and red bands, respectively, k is the slope of the soil line, and b is the interception of the soil line. The PVI was designed based on lines running perpendicular to the soil line. As pixels on a particular isoline move away from the soil line, PVI will increase from 0 to the maximum value.

2) Perpendicular Soil Moisture Index: To highlight the SM response to the evaporation of nonvegetated surface, a simple PSI, following the PDI [54], is developed by calculating the ratio of the distance between line AC and line BC in the NIR–red spectral space (Fig. 2). AC is the distance from a random pixel A in the NIR–red spectral space to the line for extremely dry bare soil (minimum SM) (CD) perpendicular to soil line ED, and BC denotes the distance between the line of wet bare soil (maximum SM) (BE) perpendicular to line ED and line CD. As shown in Fig. 2, soil line ED characterizes the variation in surface SM from maximum SM (point E), partial SM (point G), and minimum SM (point D). Thus, the PSI value of a given pixel A can be expressed as follows:

$$\text{PSI} = \frac{AC}{BC} = \frac{GD}{ED} = \frac{\rho_{d,\text{red}} - \rho_{\text{red}} + k(\rho_{d,\text{nir}} - \rho_{\text{nir}})}{\rho_{d,\text{red}} - \rho_{w,\text{red}} + k(\rho_{d,\text{nir}} - \rho_{w,\text{nir}})} \quad (2)$$

where ρ_{nir} and ρ_{red} refer to the reflectance of the NIR and red bands for pixel A, respectively, $\rho_{d,\text{nir}}$ and $\rho_{d,\text{red}}$ refer to the reflectance of the NIR and red bands for fixed pixel D with minimum SM, respectively, $\rho_{w,\text{nir}}$ and $\rho_{w,\text{red}}$ refer to the reflectance of the NIR and red bands for fixed pixel B with maximum SM, respectively, and k is the slope of the soil line. The PSI was developed based on the line that is parallel to the soil line. As pixels on a parallel line of soil line move from point C (D) to point B (E), PSI values will increase from 0 to 1.

C. NIR–Red Spectral Domain Model for LE Estimation

The NRSD model is developed based on the PT model framework by combining PVI and PSI to calculate PT parameter (Φ) to estimate daily terrestrial LE. The basic PT model
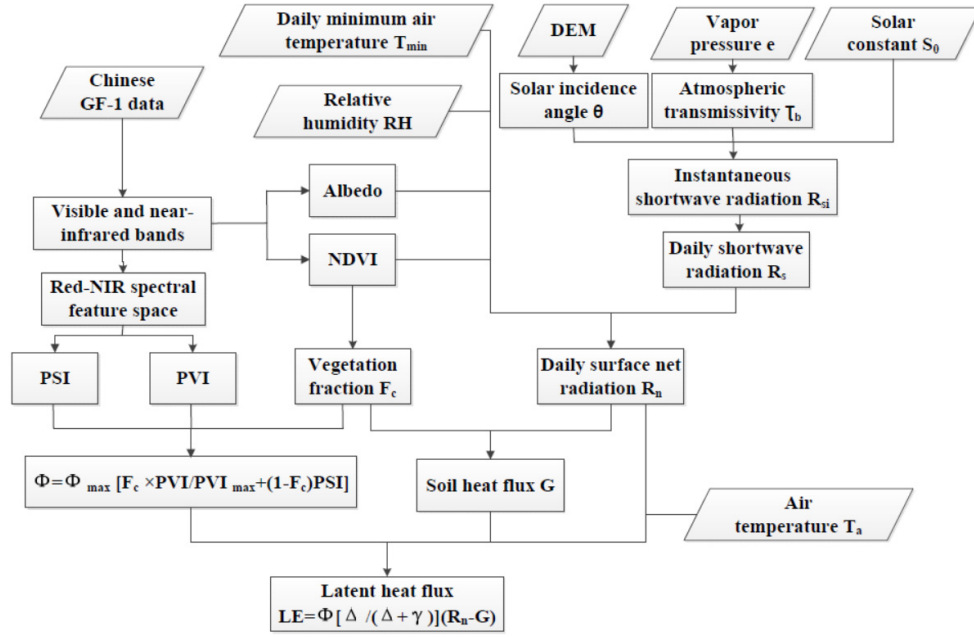
Fig. 3. Flowchart of the developed model, including inputs, intermediate variables, models, and outputs.

is expressed as follows:

$$LE = \phi \frac{\Delta}{\Delta + \gamma}(R_n - G) \quad (3)$$

where Φ is the PT parameter characterizing the actual surface resistance to LE and is generally set as 1.26 under well-watered conditions. Δ is the slope of the saturated vapor pressure curve, γ is the psychrometric constant, and R_n and G are the surface net radiation and soil heat flux, respectively.

Since PVI represents the vegetation vigor influencing vegetation transpiration while PSI reflects surface SM controlling soil evaporation, Φ can be acquired from Φ_{max} and fractional vegetation cover (F_c) by partitioning PVI and PSI. Therefore, the final equations proposed in this study are as follows:

$$\phi = \phi_{max}\left[(1 - F_c)PSI + F_c \frac{PVI}{PVI_{max}}\right] \quad (4)$$

$$F_c = \frac{NDVI - NDVI_{min}}{NDVI_{max} - NDVI_{min}} \quad (5)$$

where Φ_{max} is the maximum Φ and equals 1.26 in this study, as the maximum LE rate is assumed to occur under wet conditions. PVI_{max} is the maximum PVI during the growing season for individual pixels. $NDVI_{min}$ and $NDVI_{max}$ are the minimum and maximum NDVI for the study period set as constants of 0.05 and 0.85, respectively. In the NRSD model, Φ arrives at 1 (maximum transpiration) when F_c equals 1 because PVI arrives at PVI_{max} at this point. On the contrary, Φ equals the PSI value that varies from 0 (extremely dry bare soil and no evaporation) to 1 (wet bare soil and maximum evaporation) when F_c is set to 0. Fig. 3 shows a flowchart of the inputs, intermediate variables, outputs, and complete procedures of the NRSD model.

Daily R_n was estimated using the following equation developed by Wang and Liang [60]:

$$R_n = R_s(1 - \partial)(a_0 + a_1 T_{min} + a_2 NDVI + a_3 RH) \quad (6)$$

where $a_0 = 0.5129$, $a_1 = 0.0025$, $a_2 = 0.1401$, and $a_3 = 0.2604$. R_s is the daily surface incident shortwave radiation (W/m^2) and can be calculated using the solar constant, the relative Earth–Sun distance, the solar incidence angle, and broadband atmospheric transmissivity [31] (Appendix). T_{min} is the daily minimum air temperature. ∂ refers to the surface broadband albedo of GF-1 wide-field view (WFV) data and is retrieved using the Sun's algorithm [61]. We also used a simple empirical algorithm employing daily R_n and F_c with a fixed empirical coefficient ($a_g = 0.18$) to estimate daily soil heat flux (G) [7]

$$G = a_g(1 - F_c)R_n. \quad (7)$$

D. Comparisons to the PT-JPL Model

The PT-JPL LE model is also based on the PT model framework by including both atmospheric (RH and VPD) and ecophysiological constraints (LAI and fraction of absorbed photosynthetically active radiation, FPAR) to estimate terrestrial LE [18]. The PT-JPL model uses RH^{VPD} as an SM constraint to estimate soil evaporation under unsaturated SM conditions. The validation conducted at the 39 global flux tower sites shows that the PT-JPL model can explain more than 80% of the variation in cumulative LE with an RMSE of 13% of the observed mean [18]. PT-JPL has been widely identified as a high performing satellite LE model for multialgorithm intercomparisons [62], [63]. PT-JPL forms the core of the LE retrieval for NASA ECOSTRESS mission [49].
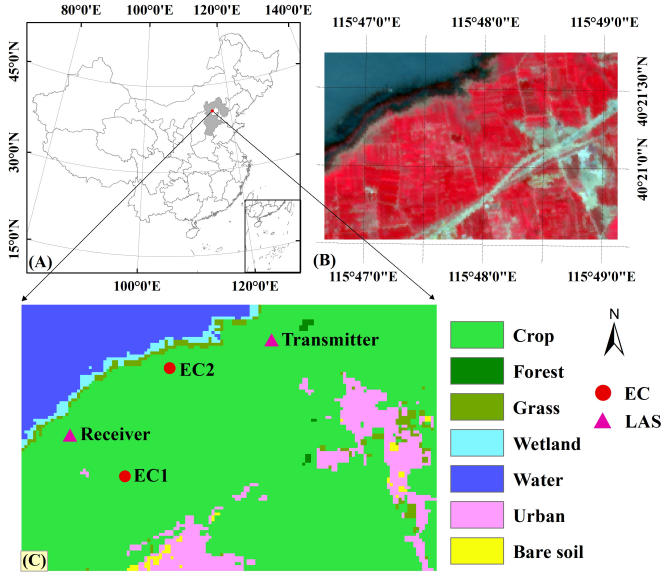
Fig. 4. Study area: (a) locations of the study area across Northern China. (b) Huailai agricultural region with a false-color composite from GF-1 imagery acquired on 9 July (DOY 190) 2017 and (c) maps of land cover types and the location of EC and LAS sites.

III. Study Area and Data Processing

A. Study Area and Flux Sites

The Huailai agricultural region is located in the Haihe River Basin of Northern China at coordinates $40.3425°$–$40.3621°$ North latitude and $115.7774°$–$115.8188°$ East longitude and covers an area of approximately 7.849 km^2 (Fig. 4). The climate of the area is semihumid and semiarid with moderate rainfall and high air temperatures occurring in the summer and little rainfall occurring during the fall and winter. The average annual temperature and precipitation are 10.5 °C and 542.5 mm, respectively. Land cover is dominated by agricultural land, with other types accounting a small portion, including forests, grassland, water bodies, wetland, bare soil, and urban areas. Agricultural land is mostly located in plains, where urbanized areas are also located. Among annual crops grown, maize is the most widespread summer crop. Forests and grasslands are mostly located in hilly areas. The cropping systems of the Huailai agricultural region are typical of agricultural features of Northern China and have substantially enhanced economic development in the region.

Both experimental test 1 (EC1, $40.3491°$N, $115.7880°$E) and experimental test 2 (EC2, $40.3574°$N, $115.7923°$E) were conducted in the western and eastern parts of the Huailai agricultural region, respectively. The two sites are governed by continuous maize within the footprint of EC towers. The height of the EC system is 10 and 40 m at the EC1 and EC2 sites, respectively. Each EC system includes a 3-D sonic anemometer (CSAT3, Campbell Scientific, Inc., Logan, UT, USA) for acquiring 3-D velocity and temperature and an open-path infrared CO_2/H_2O gas analyzer (Li-7500, Li-Cor, USA) for measuring CO_2 and H_2O density [64]–[66]. In addition, one LAS system with a transmitter ($40.3596°$N, $115.8023°$E) and receiver ($40.3522°$N, $115.7825°$E) was installed across the

EC2 tower in the north-to-south direction with the EC2 system placed in the center of the optical path of the LAS. The LAS was produced by Kipp & Zonen, Delft, The Netherlands, and the effective heights and path lengths were set to 14 and 1870 m, respectively [64], [67].

B. Eddy-Covariance and Large Aperture Scintillometer Measurements

Raw data at 10 Hz recorded by the EC systems were processed, including sonic temperatures, CO_2/H_2O lag correction relative to the vertical wind component, spike removal, and gap filling using EdiRe software (University of Edinburgh, http://www.geos.ed. ac. U.K./abs/research/micromet /EdiRe). Half-hourly turbulent surface heat fluxes (LE, R_n, H, and G) and other climate data [such as air temperature (T_a), wind speed (WS), vapor pressure (e), RH, and VPD] were acquired from both EC1 and EC2 sites. Half-hourly LE, H, G, and meteorological variables were subsequently aggregated into daily means. When missing data accounted for more than 20% of all data for a given day, the value for this day was recorded as missing. Otherwise, daily values were obtained by multiplying the averaged half-hourly rate by 48 (half hours). Due to energy imbalance, we adopted the fixed BR method [68] to correct the measured LE. As optical LAS instruments can only measure H over its path length, LE values measured from LAS instruments were calculated using the residual of the SEB equation (LE = R_n–G–H). Average R_n and G values within the calculated LAS source area footprint were acquired by weighting multiple R_n and G measurements from the EC systems [65], [69], [70].

As the footprints of the EC and LAS measurements are tens of meters and several kilometers, respectively, we used the footprint model to calculate the source area of the EC and LAS measurements. For EC measurements taken at a single point, the flux footprint, F_{EC} (m, n, z_h), was calculated based on an Eulerian analytic flux footprint model [71]

$$F_{EC}(m, n, z_h) = G_n(m, n)F^n(m, z_h) \tag{8}$$

where m is the downwind distance, n is the crosswind wind distance, z_h is the measurement height of EC, $F^n(m, z_h)$ is the crosswind integrated footprint, and $G_n(m, n)$ is the Gaussian crosswind distribution function of the lateral dispersion. By combining the path-weighting function of the LAS [72] with the above footprint function, we obtain the flux footprint [F_{LAS} (u, v, z_o)] of the LAS measurements

$$F_{LAS}(u, v, z_o) = \int_{u_2}^{u_1} H(u')F(u' - u, v' - v, z_o)du' \tag{9}$$

where $H(u')$ is the path-weighting function of the LAS, u_1 and u_2 are the locations of the LAS transmitter and receiver, respectively, z_o is the measurement height of the LAS, u' and v' denote the points along the optical length of the LAS, and u and v are the coordinates upwind of each point (u', v'). The daily flux source area of the EC and LAS measurements was determined by averaging every half-hour footprint when sensible heat fluxes were larger than 0.

To validate satellite-derived LE, we considered pixels within the source area as validation pixels, and the weighted average
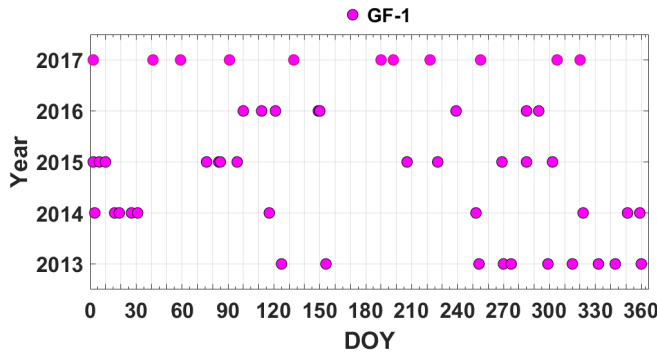
Fig. 5.   Chinese GF-1 overpass dates used for estimating daily LE over the study site during 2013–2017.

LE was obtained by summing the product of the estimated LE and relative footprint weights (i.e., the relative contribution) within each pixel

$$\text{LE}_\alpha = \sum_{i=1}^{q} (p_i \times \text{LE}_i) \tag{10}$$

where LE_a refers to the weighted average LE from remote sensing, which has the same spatial representativeness as the ground observations, p_i is the relative weight of each pixel, LE_i is the estimated LE for each pixel, and q is the number of pixels within the source area [73].

C. Chinese GF-1 and Ancillary Data

The Chinese GF-1 satellite was launched from the Jiuquan Satellite Launch Centre (Gansu Province, China) in April 2013. It is a sun-synchronous orbit satellite with two panchromatic/ multispectral (PMS) cameras and four WFV cameras that produce 16-m images every 4 days at a swath of 800 km [23]. The Chinese GF-1 WFV data include four bands: band 1 (blue: 0.45–0.52 μm), band 2 (green: 0.52–0.59 μm), band 3 (red: 0.63–0.69 μm), and band 4 (NIR: 0.77–0.89 μm). The raw Chinese GF-1 data were released as a digital number (DN) grid, and we conducted the radiance calibration to acquire surface spectral reflectance by converting the DN value of the raw image. Then, the at-surface reflectance was obtained from at-satellite reflectance based on atmospheric radiation transfer simulation models and atmospheric correction functions [74]. Finally, we used ENVI software to conduct the geometric correction, and the resampling was based on a two-order polynomial transformation by the bilinear interpolation method. We used 55 cloud-free GF-1WFV images for 2013–2017 to retrieve NDVI, PSI, and PVI (Fig. 5). Land cover maps were developed using FROM-GLC (Finer Resolution Observation and Monitoring of Global Land Cover) products with a 30-m resolution [75].

Due to the relatively homogenous atmospheric conditions within the small Huailai agricultural region, we selected *in situ* measurements of T_a, $T_{\min}$, and e as the fixed values for estimating R_n, G, and LE across this region. We also used digital elevation models (DEMs) with a 30-m spatial resolution (resampled to a 16-m resolution by linear interpolation) to
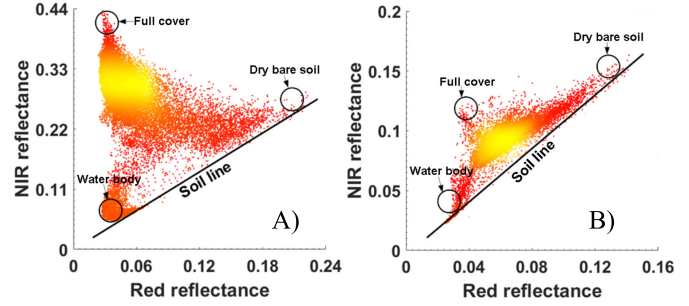

Fig. 6.   Examples of standard "NIR–red spectral space" from GF-1 data for all pixels of the study area at two different dates. (a) July 9, 2017. (b) November 1, 2017.
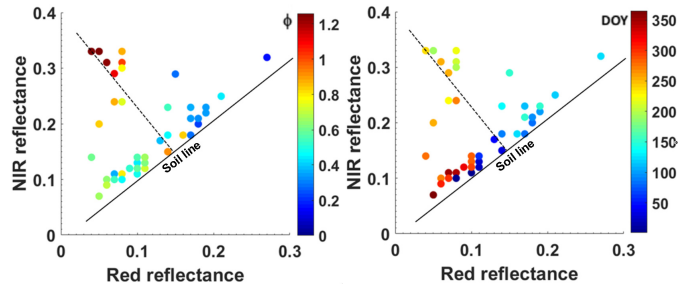

Fig. 7.   Spectral-domain-based triangle feature space for the EC1 site during the period of fluxes measurements (2014–2017): dependency of NIR–red reflectance values with the measured PT parameter Φ and DOY.

extract elevation, slope, and aspect values for estimating incident surface solar radiation (R_s).

IV. RESULTS ANALYSIS

A. Validation of the NRSD Conceptual Basis From Ground Observations

To illustrate the conceptual basis of the NRSD method, an NIR–red spectral triangular space was applied and scenes from two seasonal periods (i.e., July 9, 2017 for mid-summer and November 1, 2017 for late fall) were chosen. Fig. 6 shows the corresponding NIR–red spectral triangle shape by plotting NIR and red reflectances of GF-1 data for all pixels. Although general triangle shapes and soil lines for different scenes are easily recognizable for each date, there are great differences in the positions of the cluster pixels within the different triangles during the two growing seasons. Especially for PVI values within these two scenes, relatively high values occur in mid-summer, and low values occur in late fall. Moreover, Fig. 6 also shows that the ideal application of the NRSD method is operational only in the area of interest and includes a full range of land surface types and conditions (from water body and bare soil to full vegetation). On the contrary, the NRSD method provides a unique estimation of LE within a random pixel by determining a specific soil line, which only requires the use of the atmospheric corrected NIR, red reflectance of the study area.

An example of an NRSD scatterplot of the atmospheric corrected NIR, red reflectance from GF-1 data is plotted for the EC1 site for EC 2013–2017 observations (Fig. 7). Fig. 7
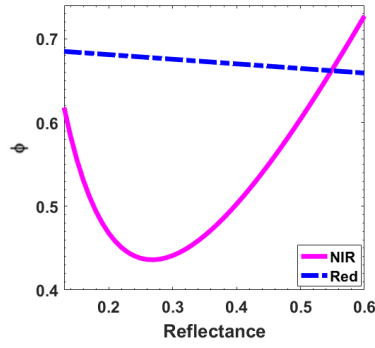
Fig. 8. Sensitivity analysis of Φ to ρ_{nir} and ρ_{red} specified between 0.13 and 0.6, incrementing by 1%.
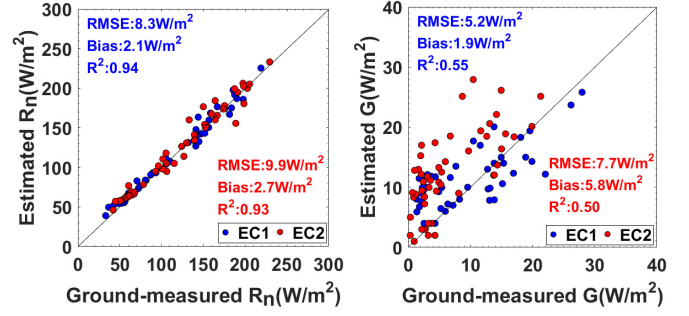

Fig. 9. Comparison of the estimated daily R_n and G values using GF-1 data with the corresponding ground measurements for the EC1 and EC2 sites.
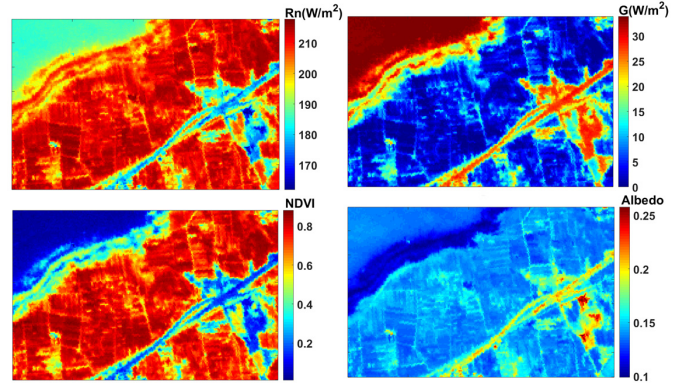

Fig. 10. Example of spatial patterns in daily R_n, G, NDVI, and Albedo of July 9, 2019.

shows the dependency of NIR–red reflectance data on the observed PT parameter Φ changes. Experimental test data scattered over the NIR–red spectral space form a triangular shape, demonstrating the presence of a soil line and its vertical lines. In the upper left vertex of the scattering, measured data points identify the maximum LE condition ($\Phi \sim 1.26$). On the contrary, data points reflect moderate LE conditions ($\Phi \sim 0.63$) in the lower left vertex of the triangle, whereas minimum LE conditions ($\Phi < 0.12$) are shown in the upper right vertex of the plot. These data points are coherent with the expected seasonal dynamics of the study areas. The flux observations collected during DOYs 150–240 (June–August) are located closer to the upper left vertex of the plot. The flux observations collected during DOYs 0–90 (January–March) and 260–350 (late September–early December) scatter in the lower left vertex of the triangle. Conversely, scattering in the upper right vertex mainly includes flux observations collected during DOYs 90–150 (March–May). The first period corresponds to the highest vegetation cover with ideal temperatures and water availability, creating the highest Φ values (>1.0). The second period reflects wet bare soil with high SM due to a low VPD, which leads to moderate LE. A high VPD and spring drought characterize the third period, localizing corresponding data points close to the upper right vertex.

For a given surface cover condition characterized by PVI within the NIR–red spectral space, the measured data points follow the expected seasonal variation under local climate conditions. Outside the growing season, with lower PVI values (<0.1), variations in the observed Φ values follow changes in PSI with the lowest Φ values observed in the spring and moderate Φ values observed in the fall and winter. On the contrary, the observed Φ changes correspond to PVI variability with the highest Φ values observed during the growing season (mainly in the summer). These reliable results support the feasibility of the NRSD method for calculating the PT parameter (Φ) to estimate agricultural regional LE.

To test the sensitivity of NRSD model to Φ, we select the EC1 site, which performs relatively better than the EC2 site, to analyze the dependence of Φ on ρ_{nir} and ρ_{red} (Fig. 8). Φ declines from 0.62 to 0.44 when ρ_{nir} increases from 0.13 to 0.3 and then Φ increases to 0.73 when ρ_{nir} reaches 0.6 and ρ_{red} is set as a constant (0.05). On the contrary, when ρ_{nir} is

set as a constant (0.5), Φ changes from 0.68 to 0.65 when ρ_{red} changes from 0.4 to 0.6. In sum, both ρ_{nir} and ρ_{red} have significant influences on Φ.

B. Evaluation of the NRSD Model

1) Modeling and validation of net radiation and soil heat flux: As both R_n and G are the critical forcing measures, we compared the estimated daily R_n and G from GF-1 data to the ground measurements. Fig. 9 shows a good agreement between the estimated daily R_n and the ground measurements. For the EC1 and EC2 sites, R^2 values obtained from comparing ground measured and estimated daily R_n values are greater than 0.92 ($p < 0.01$), whereas the RMSE values are 8.3 and 9.9 W/m^2, respectively. Moreover, the overestimations of 2.1 and 2.7 W/m^2 were observed for daily R_n at the EC1 and EC2 sites, respectively. The observed errors in estimated daily R_n appear ascribed to both systematic biases and propagated errors from the forcing data and ground measurements. On the contrary to the ground measurements, the estimated daily G yielded the R^2 values of 0.65 and 0.50 ($p < 0.01$), RMSE values of 5.2 and 7.7 W/m^2, and bias values of 1.9 and 5.8 W/m^2 for the EC1 and EC2 sites, respectively (Fig. 7). It is clear that more accurate daily G estimates were obtained for the EC1 site than for the EC2 site. This may be attributed to the use of a fixed coefficient (0.18) to estimate daily G with no adjustments in surface properties because of lacks in the sufficient data.
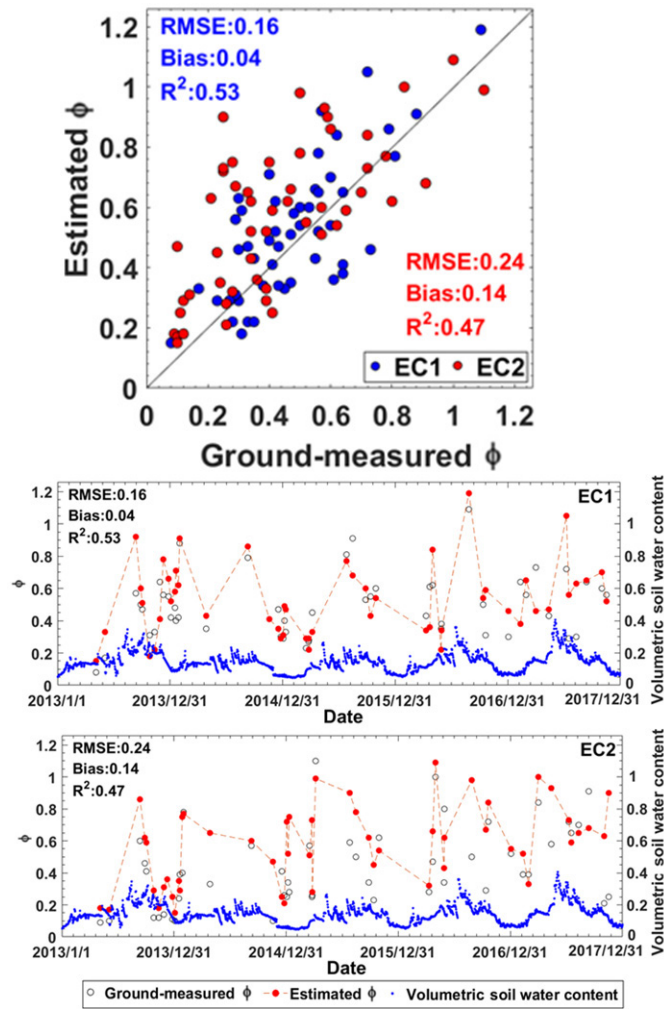
Fig. 11. Comparison of the PT parameter ϕ as measured and estimated using the NRSD model for EC1 and EC2 sites.

Fig. 12. Spatial pattern of the estimated Φ for different dates.

Fig. 10 shows an example of spatial patterns in daily R_n and G for DOY190, 2017 over the Huailai agricultural region and the corresponding NDVI and albedo values. The estimated R_n shows high values for crop fields and low values over urban areas, which is consistent with NDVI spatial patterns and runs contrary to albedo patterns. On the contrary, G maps are negatively correlated with NDVI, potentially due to the positive contributions of NDVI and negative contributions of albedo to the estimated R_n via (6), whereas (7) shows a negative NDVI contribution to the estimated G characterized by F_c.

2) Modeling and Validation of the Priestley–Taylor Coefficient: We compared the estimated PT coefficient (Φ) to the corresponding ground-measured Φ derived from LE, R_n, G, and T_a. Fig. 11 shows that the NRSD model-derived Φ estimates versus ground-measured values present similar seasonal variations and match well with the R^2 values of 0.53 and 0.47 ($p < 0.01$), RMSE values of 0.16 and 0.24, and bias values of 0.04 and 0.14 for both the EC1 and EC2 sites, respectively. In general, the Φ estimates tend toward high values in the summer due to high vegetation cover and soil water content,
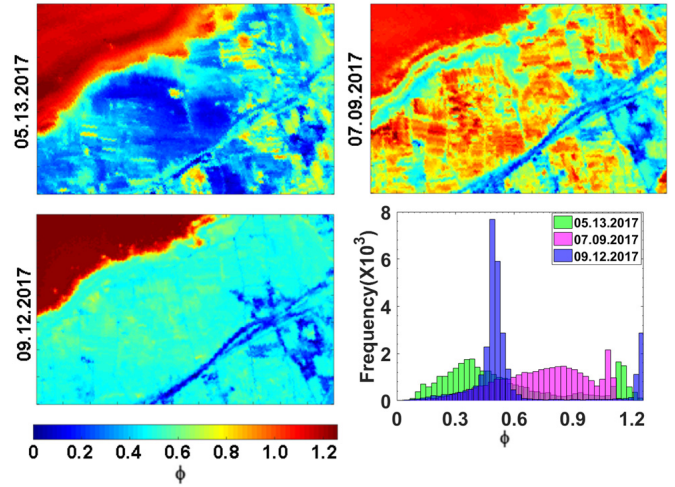
whereas low Φ values occur in the other seasons as crops are harvested and other vegetation declines.

Fig. 12 shows the spatial pattern of the estimated Φ for three days. In the top left section of the domain covered with water, the estimated Φ shows high values for 3 days. Water bodies and saturated soil in these regions may not only be accurately captured by F_c or PVI but also are characterized by PSI in real time due to the effects of moisture (Fig. 12). For other parts of the domain, the estimated Φ shows the smallest spatial variations across the images (except in the top left part of the domain), representing the narrowest spatial variations in F_c and PVI on DOY (day of year) 133. On DOY 190, spatial variations reach their highest point when F_c and PVI arrive at their maximum values. Smaller spatial variations are found on Φ maps for DOY 255 with a decrease in F_c and PVI (Figs. 12 and 13). The NRSD method, which only uses F_c and PVI sensitive to vegetation growth conditions, may not identify small differences in Φ. On the contrary, PSI's ability to account for the effect of surface SM on soil evaporation can be considered useful in compensating for the fact that PVI cannot capture bare soil information. To conclude, the strong performance of the proposed NRSD procedure confirms its reliability for practical applications.

3) Evaluation of Estimated LE Using Ground Observations and PT-JPL Model Simulations: The estimated daily LE obtained from the NRSD and PT-JPL models with a 16-m spatial resolution was validated by EC and LAS observation data, respectively. Fig. 14 shows the good agreement between EC measurements and estimates derived from the complete NRSD model for the two sites [$R^2 = 0.77$ ($p < 0.01$) and RMSE $= 17.9$ W/m^2 for site EC1 and $R^2 = 0.79$ ($p < 0.01$) and RMSE $= 21.5$ W/m^2 for site EC2]. Relative to the PT-JPL model, the average RMSE obtained from the proposed method decreases by 8.3 and 4.2 W/m^2, and R^2 increases by 0.25 and 0.14 ($p < 0.01$) for sites EC1 and EC2, respectively. Fig. 14 also shows the comparison of the estimated LE and ground measurements calculated LE from LAS data. It is clear that the NRSD model can account for 84% of LE variability
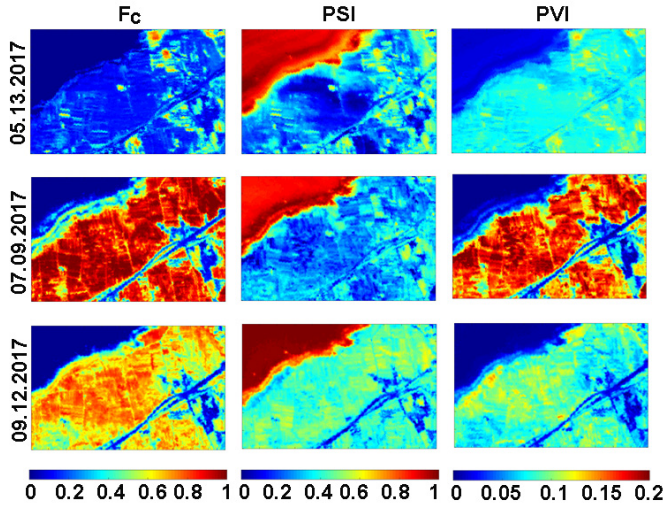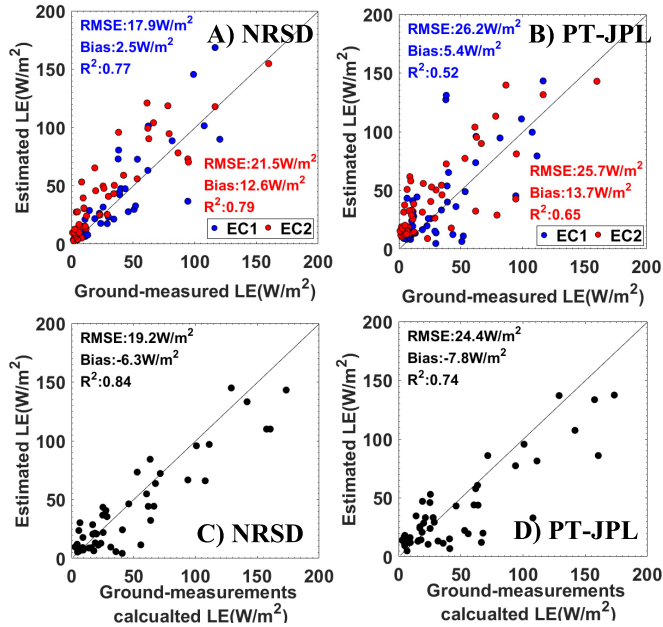
Fig. 13. Chinese GF-1-derived maps of F_c, PSI, and PVI for different dates.

Fig. 14. Comparison of the measured and estimated LE. (a) EC measured and estimated LE from NRSD model. (b) EC measured and estimated LE from PT-JPL model. (c) LAS calculated and estimated LE from NRSD model. (d) LAS calculated and estimated LE from PT-JPL model.

and that the RMSE is 19.2 W/m^2, whereas the PT-JPL model can only explain 74% of LE variability, and the RMSE is more than 24 W/m^2.

Fig. 15 shows a time series for daily LE estimates and EC measurements (and the calculated LE from LAS data) for the two EC sites (and the LAS source area). In general, the measured and estimated seasonal curves are in good agreement. In comparison to the PT-JPL model, the NRSD model yields seasonal LE variations that are closest to the EC measured values (and calculated values from LAS data). Therefore, the proposed method without calibration ranks among models that provide a better fit to EC measurements (and calculated LE from LAS data).

Fig. 16 shows the spatial distribution of daily LE estimated from the model and the PT-JPL model for 3 days. For the spring day (DOY 133), the LE estimated from the model
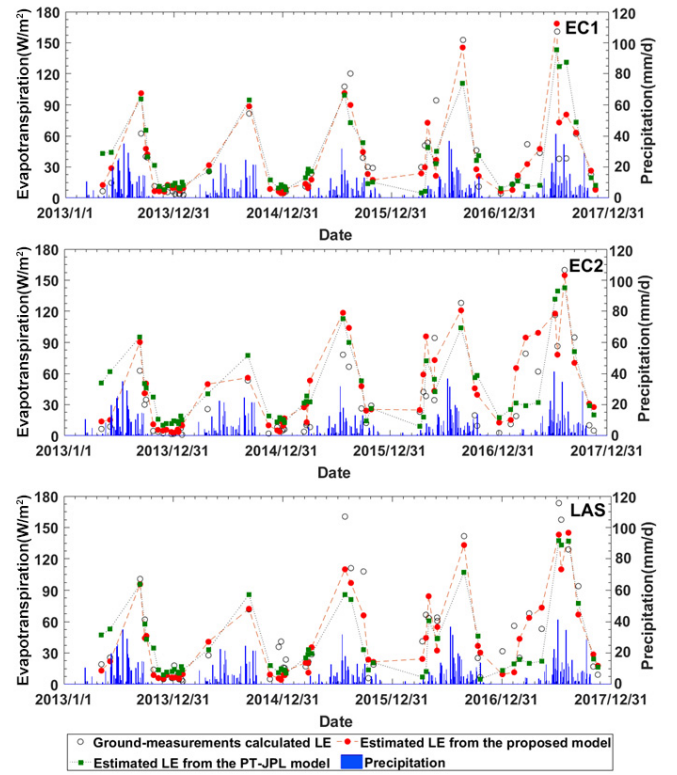

Fig. 15. Time series for daily LE estimates and EC measurements (and the calculated LE from LAS data) for two EC sites (and LAS source area).
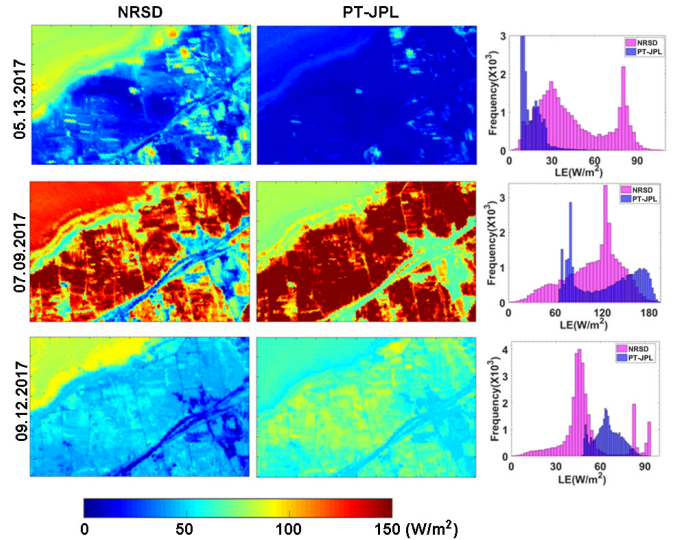

Fig. 16. Maps of LE derived from the NRSD model and the PT-JPL model for different dates, respectively.

varies from 0 to 90 W/m^2, with the highest values found in the top left part of the domain that is covered with water. However, the PT-JPL model fails identifying the water bodies for their evaporation and estimated only 0–30 W/m^2. There are modifications in place for PT-JPL to include open water evaporation as a separate retrieval routine [76]. For the summer day (DOY 190), estimated LE reaches the maximum range (0–180 W/m^2), with the smallest values in urban-dominated regions on the right and the highest values in the other regions. Meanwhile, the PT-JPL model uses meteorological variables (RH and VPD) with a coarse spatial resolution instead of

satellite reflectance data to characterize soil evaporation, and LE values estimated from the PT-JPL model range from 60 to 180 W/m^2. For the mid-fall day (DOY 255), the estimated LE is similar to values in the spring at 0–90 W/m^2, with the top left part of the domain, showing the highest LE. On the contrary, LE values estimated from the PT-JPL model are concentrated at 50–90 W/m^2 likely because the PT-JPL model fails to estimate soil and water evaporation from satellite reflectance data.

V. DISCUSSION

A. Theoretical Hypothesis for the NRSD Model

The theoretical framework of the NRSD model is the original PT equation, which determines the partitioning of available energy (R_n–G) into LE and H by adjusting the PT coefficient Φ [18], [29], [77]. The actual Φ, a key regulator for LE estimation, is generally calculated from the product of Φ_{max} (∼1.26) and ecophysiological constraints. Under unsaturated surface conditions where SM is limited, ecophysiological constraints are highly correlated with surface SM and vegetation parameters [28], [51], [78]–[80]. Here, novel ecophysiological constraints are developed using PVI and PSI retrieved from the Chinese GF-1 reflectances without auxiliary data to reflect vegetation information and surface SM for LE estimations, respectively.

Numerous studies have demonstrated that Φ values in the PT model can be considered a function of LAI (or NDVI) and SM for different biomes at the site and regional scales [81], [82]. Unfortunately, SM data sets at finer spatial resolutions are not currently available although numerous efforts have been made by taking the advantage of thermal LST data to downscale microwave SM products (e.g., SMAP) [83], [84]. However, thermal LST data not only reflect SM but also ambient atmospheric variables (e.g., T_a, RH, and WS) [85]. On the contrary, PSI retrieved from atmospheric corrected reflectances of the NIR and red bands excluding effects of ambient atmospheric variables is stable in characterizing SM and soil evaporation for a short period [54], [58]. The previous studies have also highlighted the SM deficit using the NIR–red spectral space method while neglecting soil evaporation fraction (EF$_s$) estimates [53], [57]. Here, we used PSI as a robust quantitative indicator for the effect of SM stress on LE$_s$, especially for drought periods. The PSI-based model conserves a physical characterization of soil evaporation within the PT model framework and serves as an alternative means to replace SM models to estimate agricultural field LE.

In this study, PVI offers improved crop transpiration fraction (EF$_c$) estimations because it is highly correlated with variations in vegetation water stress by adjusting vegetation densities according to environmental changes [86], [87]. Relative to NDVI, PVI saturates less for dense canopy cover, whereas NDVI saturates asymptotically [88]. Importantly, PVI appears more responsive to canopy leaf structure variations [89], and the changes in NIR reflectance are caused by the crop internal structures of leaf cells, leaf chlorophyll concentrations, and stomatal conductance [90]. Although the F_c·PVI/PVI$_{max}$ term only includes the combined effects of both PVI and NDVI on Φ, the preliminarily results confirm that the NRSD method

has ideal theoretical foundations and interpretability and yields good results.

B. Performance of the NRSD Model

1) Capacity for PSI and PVI to simulate LE: Despite its simplicity and soil line determination capacities, the NRSD model effectively estimates LE for the two case studies. The experimental findings illustrate that LE estimation using the NIR–red spectral space method markedly conserves strong correlations with ground measurements. This may be attributed to the fact that within the NRSD model, PSI synchronizes PVI but which responds differently to surface dryness that varies by water retention capacities [40], [53]. However, we found the performance of the NRSD model at site EC1 to be superior to that at site EC2 (Fig. 11). This may be partially attributed to differences in estimated available energy (R_n–G) for the two sites. The biome of the source area of the EC1 site is cropland (maize), whereas the landscape of the source area of the EC2 site includes a mixture of cropland and water bodies. Large errors will be introduced when using both (6) and (7) to calculate available energy for water bodies [7], [60].

For agricultural fields covered with annual maize, the joint use of time series PVI profiles with a fixed PVI$_{max}$ and PSI values for nonvegetation indirectly considers the effects of the mixture of cropland and other land cover types [54], [86]. This behavior is demonstrated by source area EC2, where different cover types (cropland, water bodies, and bare soil) over 5 years' result in different PSI and PVI profiles, still producing an ideal LE estimation. This underlying feature of the NRSD model can be successfully applied to complex regions that include a variety of cover types.

While the PT-JPL model performs better than most radiation-based models due to its partitioning of total LE and fewer uncertainties in driving data [61], [63], few studies have attempted on regional LE estimation at relatively high spatial resolutions (e.g., 16 m), as the PT-JPL model fails to acquire finer spatial resolution EF$_s$ from RH^{VPD}. The NRSD and PT-JPL models differ that the proposed model considers a finer spatial resolution PSI as the SM constraint to parameterize for LE$_s$ estimations [91]. This is also central to why the NRSD model performs better than the PT-JPL model as confirmed from the observation data of the EC and LAS (Figs. 11 and 12). Bei *et al.* [92] used the modified satellite-based PT (MS-PT) model and GF-1 data to estimate daily LE at the EC1 site, and their validation results show that the MS-PT model is more accurate (R^2 of more than 0.75 and RMSE of less than 20 W/m^2) and captures more detailed spatial information. The previous studies also report that at the EC1 site, TD-TESB (temperature-domain two-source energy balance model), N95-TSEB (original two-source energy balance model), and MET-RIC (satellite-based energy balance for mapping ET with internalized calibration) yield daily LE values with RMSE values of 18.9, 21.4, and 20.3 W/m^2, respectively [9]. These comparable results also illustrate the strong capacity for the NRSD model to accurately estimate agricultural field LE.

2) Uncertainties of LE Estimates: While the proposed model has been successfully extended to estimate spatially continuous LE at the agricultural field scale, errors in EC and LAS ground observations, model forcing data biases, the spatial heterogeneity of footprints of source areas (for EC and LAS) and GF-1 subpixels, and the framework of the NRSD model introduce biases into LE estimates. The EC technique is considered to be the best method for directly measuring LE at small scales (∼tens-to-hundreds of meters), but the typical error of its LE is approximately 20–50 W/m^2 [93], and gap filling from half-hour intervals to daily periods will also introduce a 5% bias into the daily LE values [94]. Unfortunately, EC measurements suffer from energy imbalances ($H+$ LE $\neq R_n - G$), and the energy closure ratio [Re $= (H+$ LE)$/(R_n - G)$] is approximately 0.8 for global FLUXNET measurements [95]. Although some scientists have attributed such energy imbalances to the fact that EC measurements only measure small eddies and ignore large eddies in the lower boundary layer and while we also correct LE in this study, errors resulting from the unclosed energy problem remain unclear [68], [93].

Biases of H measured by LAS also lead to 10%–20% errors in LE estimates [38]. An LAS will overestimate H due to the higher frictional velocity derived from Monin–Obukhov similarity theory (MOST), which constitutes the theoretical basis from which an LAS can measure H, though an LAS provides an aggregated flux over a large scale (∼ several kilometers) [96]. Furthermore, the previous studies find the great differences of approximately 20% between the results of different LASs [97]. In addition, the biases of ground-measured meteorological parameters (e.g., RH, T_a, and $T_{\min}$) and satellite-retrieved R_s, R_n, G, albedo, and F_c introduce errors into estimated LE values [1], [60]. For instance, we calculated biases in estimated daily R_n from Chinese GF-1 data at approximately 2–3 W/m^2 for the EC1 and EC2 sites, resulting in errors of more than 3 W/m^2 for daily LE estimates.

Validation from the footprints of EC and LAS observations may have partially solved the mismatch between GF-1-derived LE and ground measurements [64], [67]. However, for the Huailai agricultural region, which includes a mixture of cropland, bare soil, and water bodies (e.g., EC2), the footprints of source areas (for EC and the LAS) and GF-1 pixels exhibit subpixel heterogeneity [67], [69]. This may compromise the spatial representativeness of GF-1-derived LE and ground measurements and thereby introduce 5%–10% biases into the validation results. In addition, the framework of the NRSD model affects the accuracy of estimated LE as it does not include a modular for estimating vegetation interception evaporation, and some errors in the determination of four extreme reflectances ($\rho_{d,\mathrm{nir}}$, $\rho_{d,\mathrm{red}}$, $\rho_{w,\mathrm{nir}}$, and $\rho_{w,\mathrm{red}}$) results for PSI calculations. The use of such a simplified model for agricultural application may lead to uncertainties in LE estimates.

C. Strengths and Limitations of the NRSD Model

Compared to the other extended PT models, the NRSD model offers three significant benefits. First, it improves model operability for estimating agricultural field LE because it only requires the reflectance of the NIR and red bands to calculate PT coefficients and thus does not require the use of SM data. Currently, reliable SM data sets necessary for optimizing PT coefficients in many models are not available at finer scales [17], [85]. Second, the model provides an estimation of total LE partitioned to the vegetation canopy (LE$_c$) and soil (LE$_s$) though we did not validate LE$_c$ and LE$_s$ due to a lack of sufficient auxiliary data. PSI in the NRSD model serves as an alternative LE$_s$ estimation tool for satellites without thermal LST data, and PVI saturates less in dense vegetation cover than NDVI, which can offer a physical characterization of LE$_c$. Finally, the NRSD model is robust and reliable when compared to ground measurements and other extended PT models.

Similar to the other triangular or trapezoidal methods, the NRSD model has three distinct limitations. First, it ignores vegetation interception loss, which accounts for 8%–40% of annual gross precipitation [98] and which may result in considerable LE underestimations for humid environments. The satellite-based Gash model [98], which replaces canopy interception with the interception of vegetation and considers subpixel heterogeneity based on a Poisson distribution function for the LAI value of each pixel, can be applied to accurately estimate vegetation interception loss, which will be pursued in the ongoing work. Second, the model employs subjectivity in determining soil line and bare soil extremes in identifying $\rho_{d,\mathrm{nir}}$, $\rho_{d,\mathrm{red}}$, $\rho_{w,\mathrm{nir}}$, and $\rho_{w,\mathrm{red}}$. As the reflectance of the NIR and red bands varies greatly with complex land surface conditions, we visually inspected NIR–red spectral spaces to extract soil line and bare soil extremes, though this may still lead to approximately 10% errors in LE estimates. Finally, the NRSD model may not be applied to areas without a full range of land surface types and conditions, as a triangle of NIR–red spectral space is not present, constraining the calculation of PSI and PVI. Further efforts should focus on the development of surface property reference tables to improve the performance of the NRSD model.

VI. Conclusion

We propose an NRSD model by combining PVI and PSI values from Chinese GF-1 data to calculate PT parameters (Φ) in estimating daily terrestrial LE. In the NRSD model, PVI characterizes vegetation vigor to determine vegetation transpiration, whereas PSI reflects surface SM controlling soil evaporation, especially when using the Chinese GF-1 satellite. Validations conducted at two EC sites and one LAS station in the Huailai agricultural region of China and 55 scenes of Chinese GF-1 WFV data illustrate that the NRSD model performed well. Overall, the R^2 (99% confidence) of the estimated versus ground-measured daily LE is 0.77 and 0.79 and the RMSE is 17.9 and 21.5 W/m^2 for sites EC1 and EC2, respectively. The site-calibrated statistics are improved by 0.14–0.25 for R^2 and decreased by 4.2–8.3 W/m^2 for RMSE as compared to the commonly used universal PT-JPL model. For the LAS site, the NRSD model can account for 84% of LE variability and that the RMSE is 19.2 W/m^2, whereas the PT-JPL model can only explain 74% of LE variability and the RMSE is more than 24 W/m^2. This study thus provides an alternative model for estimating regional LE and describes

modes high spatial resolution LE_s estimation from NIR–red spectral spaces for areas lacking thermal satellite data.

APPENDIX: R_s ESTIMATION

Instantaneous surface incident shortwave radiation (R_{si}) is the principal energy source for R_n estimation and can be calculated as follows using the solar constant (S_0, 1367 W/m^2), relative Earth–Sun distance (d_e), solar incidence angle (θ), and broadband atmospheric transmissivity (τ_b):

$$R_{si} = \frac{S_0 \cos\theta \tau_b}{d_e^2} \qquad (A1)$$

where R_{si} values estimated have been validated to be at least as accurate as R_{si} values measured by automated weather station [31], whereas τ_b is calculated based on a general function given by the ASCE-EWRI, which has been described elsewhere [31], [35]. Daily surface incident shortwave radiation (R_s) is calculated using a sinusoidal curve interpolation method based on the sinusoidal curve of the variation in solar altitude over the course of a day.

ACKNOWLEDGMENT

REFERENCES

[1] J. B. Fisher et al., "The future of evapotranspiration: Global requirements for ecosystem functioning, carbon and climate feedbacks, agricultural management, and water resources," Water Resour. Res., vol. 53, no. 4, pp. 2618–2626, Apr. 2017.

[2] S. Liang, K. Wang, X. Zhang, and M. Wild, "Review on estimation of land surface radiation and energy budgets from ground measurement, remote sensing and model simulations," IEEE J. Sel. Topics Appl. Earth Observ. Remote Sens., vol. 3, no. 3, pp. 225–240, Sep. 2010.

[3] M. Jung et al., "Recent decline in the global land evapotranspiration trend due to limited moisture supply," Nature, vol. 467, no. 7318, pp. 951–954, Oct. 2010.

[4] M. F. McCabe, B. Aragon, R. Houborg, and J. Mascaro, "CubeSats in hydrology: Ultrahigh-resolution insights into vegetation dynamics and terrestrial evaporation," Water Resour. Res., vol. 53, no. 12, pp. 10017–10024, Dec. 2017.

[5] T. R. McVicar and D. L. B. Jupp, "Using covariates to spatially interpolate moisture availability in the Murray–Darling basin," Remote Sens. Environ., vol. 79, nos. 2–3, pp. 199–212, Feb. 2002.

[6] Q. Mu, F. A. Heinsch, M. Zhao, and S. W. Running, "Development of a global evapotranspiration algorithm based on MODIS and global meteorology data," Remote Sens. Environ., vol. 111, no. 4, pp. 519–536, Dec. 2007.

[7] Y. Yao et al., "MODIS-driven estimation of terrestrial latent heat flux in China based on a modified Priestley–Taylor algorithm," Agricult. Forest Meteorol., vols. 171–172, pp. 187–202, Apr. 2013.

[8] X. Hu, L. Shi, L. Lin, B. Zhang, and Y. Zha, "Optical-based and thermal-based surface conductance and actual evapotranspiration estimation, an evaluation study in the North China plain," Agricult. Forest Meteorol., vol. 263, pp. 449–464, Dec. 2018.

[9] Y. Yao et al., "A simple temperature domain two-source model for estimating agricultural field surface energy fluxes from Landsat images," J. Geophys. Res. Atmos., vol. 122, no. 10, pp. 5211–5236, May 2017.

[10] D. Baldocchi et al., "FLUXNET: A new tool to study the temporal and spatial variability of ecosystem-scale carbon dioxide, water vapor, and energy flux densities," Bull. Amer. Meteorological Soc., vol. 82, no. 82, pp. 2415–2434, 2001.

[11] G. Hu and L. Jia, "Monitoring of evapotranspiration in a semi-arid inland river basin by combining microwave and optical remote sensing observations," Remote Sens., vol. 7, no. 3, pp. 3056–3087, Mar. 2015.

[12] S. Liu et al., "The heihe integrated observatory network: A basin-scale land surface processes observatory in China," Vadose Zone J., vol. 17, no. 1, 2018, Art. no. 180072.

[13] B. R. Scanlon, S. W. Tyler, and P. J. Wierenga, "Hydrologic issues in arid, unsaturated systems and implications for contaminant transport," Rev. Geophys., vol. 35, no. 4, pp. 461–490, Nov. 1997.

[14] R. Tang, Z. Li, and B. Tang, "An application of the Ts-VI triangle method with enhanced edges determination for evapotranspiration estimation from MODIS data in arid and semi-arid regions: Implementation and validation," Remote Sens. Environ., vol. 114, no. 3, pp. 540–551, 2010.

[15] K. Wang and S. Liang, "An improved method for estimating global evapotranspiration based on satellite determination of surface net radiation, vegetation index, temperature, and soil moisture," J. Hydrometeorol., vol. 9, no. 4, pp. 712–727, Aug. 2008.

[16] J. Xu et al., "Merging the MODIS and Landsat terrestrial latent heat flux products using the multiresolution tree method," IEEE Trans. Geosci. Remote Sens., vol. 57, no. 5, pp. 2811–2823, May 2019.

[17] M. Anderson, J. Norman, W. Kustas, R. Houborg, P. Starks, and N. Agam, "A thermal-based remote sensing technique for routine mapping of land-surface carbon, water and energy fluxes from field to regional scales," Remote Sens. Environ., vol. 112, no. 12, pp. 4227–4241, Dec. 2008.

[18] J. B. Fisher, K. P. Tu, and D. D. Baldocchi, "Global estimates of the land–atmosphere water flux based on monthly AVHRR and ISLSCP-II data, validated at 16 FLUXNET sites," Remote Sens. Environ., vol. 112, no. 3, pp. 901–919, Mar. 2008.

[19] J. D. Kalma, T. R. McVicar, and M. F. McCabe, "Estimating land surface evaporation: A review of methods using remotely sensed surface temperature data," Surv. Geophys., vol. 29, nos. 4–5, pp. 421–469, Oct. 2008.

[20] W. P. Kustas and J. M. Norman, "Evaluation of soil and vegetation heat flux predictions using a simple two-source model with radiometric temperatures for partial canopy cover," Agricult. Forest Meteorol., vol. 94, no. 1, pp. 13–29, Apr. 1999.

[21] S. O. Los et al., "A global 9-yr biophysical land surface dataset from NOAA AVHRR data," J. Hydrometeorol., vol. 1, no. 2, pp. 183–199, Apr. 2000.

[22] Q. Mu, M. Zhao, and S. W. Running, "Improvements to a MODIS global terrestrial evapotranspiration algorithm," Remote Sens. Environ., vol. 115, no. 8, pp. 1781–1800, Aug. 2011.

[23] K. Jia et al., "Fractional vegetation cover estimation algorithm for chinese GF-1 wide field view data," Remote Sens. Environ., vol. 177, pp. 184–191, May 2016.

[24] J. M. Norman, W. P. Kustas, and K. S. Humes, "Source approach for estimating soil and vegetation energy fluxes in observations of directional radiometric surface temperature," Agricult. Forest Meteorol., vol. 77, nos. 3–4, pp. 263–293, Dec. 1995.

[25] G. Y. Qiu, P. Shi, and L. Wang, "Theoretical analysis of a remotely measurable soil evaporation transfer coefficient," Remote Sens. Environ., vol. 101, no. 3, pp. 390–398, Apr. 2006.

[26] J. Cheng and W. Kustas, "Using very high resolution thermal infrared imagery for more accurate determination of the impact of land cover differences on evapotranspiration in an irrigated agricultural area," Remote Sens., vol. 11, no. 6, p. 613, Mar. 2019.

[27] E. P. Glenn, P. L. Nagler, and A. R. Huete, "Vegetation index methods for estimating evapotranspiration by remote sensing," *Surv. Geophys.*, vol. 31, no. 6, pp. 531–555, Dec. 2010.

[28] K. Wang, R. Dickinson, M. Wild, and S. Liang, "Evidence for decadal variation in global terrestrial evapotranspiration between 1982 and 2002: 1. Model development," *J. Geophys. Res.*, vol. 115, Oct. 2010, Art. no. D20112.

[29] Y. Yao *et al.*, "A satellite-based hybrid algorithm to determine the Priestley–Taylor parameter for global terrestrial latent heat flux estimation across multiple biomes," *Remote Sens. Environ.*, vol. 165, pp. 216–233, Aug. 2015.

[30] M. Yebra, A. Van Dijk, R. Leuning, A. Huete, and J. P. Guerschman, "Evaluation of optical remote sensing to estimate actual evapotranspiration and canopy conductance," *Remote Sens. Environ.*, vol. 129, pp. 250–261, Feb. 2013.

[31] R. G. Allen, M. Tasumi, and R. Trezza, "Satellite-based energy balance for mapping evapotranspiration with internalized calibration (METRIC)—Model," *J. Irrigation Drainage Eng.*, vol. 133, no. 4, pp. 380–394, Aug. 2007.

[32] W. G. M. Bastiaanssen, M. Menenti, R. A. Feddes, and A. A. M. Holtslag, "A remote sensing surface energy balance algorithm for land (SEBAL). 1. Formulation," *J. Hydrol.*, vols. 212–213, pp. 198–212, Dec. 1998.

[33] Z. Su, "The surface energy balance system (SEBS) for estimation of turbulent heat fluxes," *Hydrol. Earth Syst. Sci.*, vol. 6, no. 1, pp. 85–100, Feb. 2002.

[34] T. Carlson, "An overview of the 'triangle method' for estimating surface evapotranspiration and soil moisture from satellite imagery," *Sensors*, vol. 7, no. 8, pp. 1612–1629, Aug. 2007.

[35] D. Long and V. P. Singh, "A Two-source trapezoid model for evapotranspiration (TTME) from satellite imagery," *Remote Sens. Environ.*, vol. 121, pp. 370–388, Jun. 2012.

[36] Y. Yang and S. Shang, "A hybrid dual-source scheme and trapezoid framework-based evapotranspiration model (HTEM) using satellite images: Algorithm and model test," *J. Geophys. Res. Atmos.*, vol. 118, no. 5, pp. 2284–2300, Mar. 2013.

[37] Z.-L. Li *et al.*, "A review of current methodologies for regional evapotranspiration estimation from remotely sensed data," *Sensors*, vol. 9, no. 5, pp. 3801–3853, May 2009.

[38] K. Wang and R. E. Dickinson, "A review of global terrestrial evapotranspiration: Observation, modeling, climatology, and climatic variability," *Rev. Geophys.*, vol. 50, no. 2, 2012, Art. no. RG2005.

[39] K. Zhang, J. S. Kimball, and S. W. Running, "A review of remote sensing based actual evapotranspiration estimation," *Wiley Interdiscipl. Rev. Water*, vol. 3, no. 6, pp. 834–853, Nov. 2016.

[40] F. Maselli *et al.*, "Operational monitoring of daily evapotranspiration by the combination of MODIS NDVI and ground meteorological data: Application and evaluation in central Italy," *Remote Sens. Environ.*, vol. 152, pp. 279–290, Sep. 2014.

[41] T. Xu, S. Liu, S. Liang, and J. Qin, "Improving predictions of water and heat fluxes by assimilating MODIS land surface temperature products into common land model," *J. Hydrometeorol.*, vol. 12, no. 2, pp. 227–244, 2011.

[42] A. Polhamus, J. B. Fisher, and K. P. Tu, "What controls the error structure in evapotranspiration models?" *Agricult. Forest Meteorol.*, vol. 169, pp. 12–24, Feb. 2013.

[43] M. C. Anderson, R. G. Allen, A. Morse, and W. P. Kustas, "Use of Landsat thermal imagery in monitoring evapotranspiration and managing water resources," *Remote Sens. Environ.*, vol. 122, pp. 50–65, Jul. 2012.

[44] M. Marshall, K. Tu, and V. Andreo, "On parameterizing soil evaporation in a direct remote sensing model of ET: PT-JPL," *Water Resour. Res.*, vol. 56, no. 5, 2020, Art. no. e2019WR026290.

[45] D. G. Miralles, T. R. H. Holmes, R. A. M. De Jeu, J. H. Gash, A. G. C. A. Meesters, and A. J. Dolman, "Global land-surface evaporation estimated from satellite-based observations," *Hydrol. Earth Syst. Sci.*, vol. 15, no. 2, pp. 453–469, Feb. 2011.

[46] E. P. Glenn *et al.*, "Actual evapotranspiration estimation by ground and remote sensing methods: The Australian experience," *Hydrological Processes*, vol. 25, no. 26, pp. 4103–4116, Dec. 2011.

[47] E. King, *et al.*, *Actual Evapotranspiration Estimates for Australia Intercomparison and Evaluation*, In C.W.f.a.H.C.N.R. Flagship, Ed. Canberra, ACT, Australia, 2011.

[48] H. A. Cleugh, R. Leuning, Q. Mu, and S. W. Running, "Regional evaporation estimates from flux tower and MODIS satellite data," *Remote Sens. Environ.*, vol. 106, no. 3, pp. 285–304, Feb. 2007.

[49] J. B. Fisher *et al.*, "ECOSTRESS: NASA's next generation mission to measure evapotranspiration from the international space station," *Water Resour. Res.*, vol. 56, no. 4, pp. 1–20, 2020.

[50] P. L. Nagler, J. Cleverly, E. Glenn, D. Lampkin, A. Huete, and Z. Wan, "Predicting riparian evapotranspiration from MODIS vegetation indices and meteorological data," *Remote Sens. Environ.*, vol. 94, no. 1, pp. 17–30, Jan. 2005.

[51] A. J. Purdy *et al.*, "SMAP soil moisture improves global evapotranspiration," *Remote Sens. Environ.*, vol. 219, pp. 1–14, Dec. 2018.

[52] H. Yan and H. H. Shugart, "An air relative-humidity-based evapotranspiration model from eddy covariance data," *J. Geophys. Res.*, vol. 115, no. D16, 2010, Art. no. D16106.

[53] M. Amani, B. Salehi, S. Mahdavi, A. Masjedi, and S. Dehnavi, "Temperature-vegetation-soil moisture dryness index (TVMDI)," *Remote Sens. Environ.*, vol. 197, pp. 1–14, Aug. 2017.

[54] A. Ghulam, Q. Qin, and Z. Zhan, "Designing of the perpendicular drought index," *Environ. Geol.*, vol. 52, no. 6, pp. 1045–1052, May 2007.

[55] A. Ghulam, Q. Qin, T. Teyip, and Z.-L. Li, "Modified perpendicular drought index (MPDI): A real-time drought monitoring method," *ISPRS J. Photogramm. Remote Sens.*, vol. 62, no. 2, pp. 150–164, Jun. 2007.

[56] M. Sadeghi, E. Babaeian, M. Tuller, and S. B. Jones, "The optical trapezoid model: A novel approach to remote sensing of soil moisture applied to Sentinel-2 and Landsat-8 observations," *Remote Sens. Environ.*, vol. 198, pp. 52–68, Sep. 2017.

[57] Q. Qin, C. Jin, N. Zhang, and X. Yang, "An two-dimensional spectral space based model for drought monitoring and its re-examination," in *Proc. IEEE Int. Geosci. Remote Sens. Symp. (IGARSS)*, Jul. 2010, pp. 3869–3872.

[58] M. Amani, S. Parsian, S. M. Mirmazloumi, and O. Aieneh, "Two new soil moisture indices based on the NIR-red triangle space of Landsat-8 data," *Int. J. Appl. Earth Observ. Geoinf.*, vol. 50, pp. 176–186, Aug. 2016.

[59] A. J. Richardson and C. L. Wiegand, "Distinguishing vegetation from soil background information," *Photogramm. Eng. Remote Sens.*, vol. 43, no. 12, pp. 1541–1552, 1977.

[60] K. Wang and S. Liang, "Estimation of daytime net radiation from shortwave radiation measurements and meteorological observations," *J. Appl. Meteorol. Climatol.*, vol. 48, no. 3, pp. 634–643, Mar. 2009.

[61] Y. J. Sun, Z. H. Wang, Q. M. Qin, G. H. Han, H. Z. Ren, and J. F. Huang, "Retrieval of surface albedo based on GF-4 geostationary satellite image data," *J. Remote Sens.*, vol. 22, no. 2, pp. 220–233, 2018.

[62] R. K. Vinukollu, E. F. Wood, C. R. Ferguson, and J. B. Fisher, "Global estimates of evapotranspiration for climate studies using multi-sensor remote sensing data: Evaluation of three process-based approaches," *Remote Sens. Environ.*, vol. 115, no. 3, pp. 801–823, Mar. 2011.

[63] A. Ershadi, M. F. McCabe, J. P. Evans, N. W. Chaney, and E. F. Wood, "Multi-site evaluation of terrestrial evaporation models using FLUXNET data," *Agricult. Forest Meteorol.*, vol. 187, pp. 46–61, Apr. 2014.

[64] S. M. Liu, Z. W. Xu, Z. L. Zhu, Z. Z. Jia, and M. J. Zhu, "Measurements of evapotranspiration from eddy-covariance systems and large aperture scintillometers in the Hai River Basin, China," *J. Hydrol.*, vol. 487, pp. 24–38, Apr. 2013.

[65] S. Liu *et al.*, "Upscaling evapotranspiration measurements from multi-site to the satellite pixel scale over heterogeneous land surfaces," *Agricult. Forest Meteorol.*, vol. 230, pp. 97–113, 2016.

[66] Z. Xu *et al.*, "Intercomparison of surface energy flux measurement systems used during the HiWATER-MUSOEXE," *J. Geophys. Res.*, vol. 118, no. 23, pp. 13140–13157, 2013.

[67] Z. Jia, S. Liu, Z. Xu, Y. Chen, and M. Zhu, "Validation of remotely sensed evapotranspiration over the Hai River Basin, China," *J. Geophys. Res. Atmos.*, vol. 117, no. D13, Jul. 2012, Art. no. D13113.

[68] T. E. Twine *et al.*, "Correcting eddy-covariance flux underestimates over a grassland," *Agricult. Forest Meteorol.*, vol. 103, no. 3, pp. 279–300, Jun. 2000.

[69] L. Song *et al.*, "Monitoring and validating spatially and temporally continuous daily evaporation and transpiration at river basin scale," *Remote Sens. Environ.*, vol. 219, pp. 72–88, Dec. 2018.

[70] H. M. Hemakumara, L. Chandrapala, and A. F. Moene, "Evapotranspiration fluxes over mixed vegetation areas measured from large aperture scintillometer," *Agricult. Water Manage.*, vol. 58, no. 2, pp. 109–122, Feb. 2003.

[71] R. Kormann and F. Meixner, "An analytical footprint model for non-neutral stratification," *Boundary-Layer Meteorol.*, vol. 99, no. 2, pp. 207–224, 2001.

[72] W. M. L. Meijninger, O. K. Hartogensis, W. Kohsiek, J. C. B. Hoedjes, R. M. Zuurbier, and H. A. R. De Bruin, "Determination of area-averaged sensible heat fluxes with a large aperture scintillometer over a heterogeneous surface—Flevoland field experiment," *Boundary-Layer Meteorol.*, vol. 105, no. 1, pp. 37–62, Oct. 2002.

[73] V. Giannico, J. Chen, C. Shao, Z. Ouyang, R. John, and R. Lafortezza, "Contributions of landscape heterogeneity within the footprint of eddy-covariance towers to flux measurements," *Agricult. Forest Meteorol.*, vol. 260, pp. 144–153, Oct. 2018.

[74] M. Tasumi, R. G. Allen, and R. Trezza, "At-surface reflectance and albedo from satellite for operational calculation of land surface energy balance," *J. Hydrologic Eng.*, vol. 13, no. 2, pp. 51–63, Feb. 2008.

[75] P. Gong et al., "Finer resolution observation and monitoring of global land cover: First mapping results with Landsat TM and ETM+ data," *Int. J. Remote Sens.*, vol. 34, no. 7, pp. 2607–2654, 2013.

[76] M. Dohlen, J. B. Fisher, G. H. Halverson, J. Collison, and J. L. Huntington, "Remotely sensed open water reservoir and lake evaporation," Amer. Geophys. Union, San Francisco, CA, USA, Tech. Rep. 15, 2019.

[77] C. H. B. Priestley and R. J. Taylor, "On the assessment of surface heat flux and evaporation using large-scale parameters," *Monthly Weather Rev.*, vol. 100, no. 2, pp. 81–92, Feb. 1972.

[78] L. Wang, O. Kisi, M. Zounemat-Kermani, and H. Li, "Pan evaporation modeling using six different heuristic computing methods in different climates of China," *J. Hydrol.*, vol. 544, pp. 407–427, Jan. 2017.

[79] L. Wang, O. Kisi, B. Hu, M. Bilal, M. Zounemat-Kermani, and H. Li, "Evaporation modelling using different machine learning technique," *Int. J. Climatol.*, vol. 37, no. s1, pp. 1076–1092, 2017.

[80] L. Wang, Z. Niu, O. Kisi, C. Li, and D. Yu, "Pan evaporation modeling using four different heuristic approaches," *Comput. Electron. Agricult.*, vol. 140, pp. 203–213, Aug. 2017.

[81] Y. Yao et al., "Evaluation of a satellite-derived model parameterized by three soil moisture constraints to estimate terrestrial latent heat flux in the Heihe River Basin of Northwest China," *Sci. Total Environ.*, vol. 695, Dec. 2019, Art. no. 133787.

[82] Y. Jin, J. T. Randerson, and M. L. Goulden, "Continental-scale net radiation and evapotranspiration estimated using MODIS satellite observations," *Remote Sens. Environ.*, vol. 115, no. 9, pp. 2302–2319, Sep. 2011.

[83] S. Gao, Z. Zhu, H. Weng, and J. Zhang, "Upscaling of sparse in situ soil moisture observations by integrating auxiliary information from remote sensing," *Int. J. Remote Sens.*, vol. 38, no. 17, pp. 4782–4803, Sep. 2017.

[84] T. R. H. Holmes, C. R. Hain, W. T. Crow, M. C. Anderson, and W. P. Kustas, "Microwave implementation of two-source energy balance approach for estimating evapotranspiration," *Hydrol. Earth Syst. Sci.*, vol. 22, no. 2, pp. 1351–1369, Feb. 2018.

[85] K. Mallick, B. K. Bhattacharya, and N. K. Patel, "Estimating volumetric surface moisture content for cropped soils using a soil wetness index based on surface temperature and NDVI," *Agricult. Forest Meteorol.*, vol. 149, no. 8, pp. 1327–1342, Aug. 2009.

[86] S. Saidi, D. Louppe, and S. L. Bel, "Estimating tree density with the perpendicular vegetation index: Application to the tree Savannahs of Northern Tanzania," *Bois et Forets des Tropiques*, vol. 337, pp. 39–51, 2018.

[87] B. Sharma, G. L. Ritchie, and N. Rajan, "Near-remote green: Red perpendicular vegetation index ground cover fraction estimation in cotton," *Crop Sci.*, vol. 55, no. 5, pp. 2252–2261, Sep. 2015.

[88] A. Huete, K. Didan, T. Miura, E. P. Rodriguez, X. Gao, and L. G. Ferreira, "Overview of the radiometric and biophysical performance of the MODIS vegetation indices," *Remote Sens. Environ.*, vol. 83, nos. 1–2, pp. 195–213, Nov. 2002.

[89] L. Grant, "Diffuse and specular characteristics of leaf reflectance," *Remote Sens. Environ.*, vol. 22, no. 2, pp. 309–322, Jul. 1987.

[90] K. Matsumoto, T. Ohta, and T. Tanaka, "Dependence of stomatal conductance on leaf chlorophyll concentration and meteorological variables," *Agricult. Forest Meteorol.*, vol. 132, nos. 1–2, pp. 44–57, Sep. 2005.

[91] B. Aragon, R. Houborg, K. Tu, J. B. Fisher, and M. McCabe, "CubeSats enable high spatiotemporal retrievals of crop-water use for precision agriculture," *Remote Sens.*, vol. 10, no. 12, p. 1867, Nov. 2018.

[92] X. Bei et al., "Estimation of daily terrestrial latent heat flux with high spatial resolution from MODIS and Chinese GF-1 data," *Sensors*, vol. 20, no. 10, p. 2811, 2020.

[93] T. Foken, "The energy balance closure problem: An overview," *Ecol. Appl. A Publication Ecol. Soc. Amer.*, vol. 18, no. 6, pp. 1351–1367, 2008.

[94] E. Falge et al., "Gap filling strategies for long term energy flux data sets," *Agricult. Forest Meteorol.*, vol. 107, no. 1, pp. 71–77, Mar. 2001.

[95] K. Wilson et al., "Energy balance closure at FLUXNET sites," *Agricult. Forest Meteorol.*, vol. 113, nos. 1–4, pp. 223–243, Dec. 2002.

[96] X. Zhang, X. Jia, J. Yang, and L. Hu, "Evaluation of MOST functions and roughness length parameterization on sensible heat flux measured by large aperture scintillometer over a corn field," *Agricult. Forest Meteorol.*, vol. 150, no. 9, pp. 1182–1191, Aug. 2010.

[97] J. Kleissl, J. Gomez, S.-H. Hong, J. M. H. Hendrickx, T. Rahn, and W. L. Defoor, "Large aperture scintillometer intercomparison study," *Boundary-Layer Meteorol.*, vol. 128, no. 1, pp. 133–150, Jul. 2008.

[98] J. H. C. Gash, C. R. Lloyd, and G. Lachaud, "Estimating sparse forest rainfall interception with an analytical model," *J. Hydrol.*, vol. 170, nos. 1–4, pp. 79–86, Aug. 1995.

Yunjun Yao received the Ph.D. degree from Peking University, Beijing, China, in 2010.

From 2008 to 2009, he was a Joint Ph.D. Student with the Department of Geographical Sciences, University of Maryland, College Park, MD, USA. He is an Associate Professor with the State Key Laboratory of Remote Sensing Science, Faculty of Geographical Science, Beijing Normal University, Beijing. His research interests include the estimation of evapotranspiration and retrieval of surface biophysical parameters by remote sensing.

Shunlin Liang (Fellow, IEEE) received the Ph.D. degree from Boston University, Boston, MA, USA.

He is a Professor with the Department of Geographical Sciences, University of Maryland, College Park, MD, USA. He has authored over 360 SCI indexed peer-reviewed journal articles, 42 book chapters, and 9 special issues of different journals. He authored/edited seven books, four of which were translated in Chinese, such as *Quantitative Remote Sensing of Land Surfaces* (Wiley, 2004), *Advances in Land Remote Sensing: System, Modeling, Inversion and Application* (Springer, 2008), *Advanced Remote Sensing: Terrestrial Information Extraction and Applications* (Academic Press, 2012 and 2019), *Global LAnd Surface Satellite (GLASS) Products: Algorithms, Validation and Analysis* (Springer, 2013), *Land Surface Observation, Modeling And Data Assimilation* (World Scientific, 2013), and *Earth's Energy Budget* (Elsevier, 2017). His main research interests focus on estimation of land surface variables from satellite data, Earth's energy balance, and assessment of environmental changes.

Dr. Liang was the Editor-in-Chief of the nine-volume series *Comprehensive Remote Sensing* (Elsevier, 2017). He was an Associate Editor of the IEEE TRANSACTIONS ON GEOSCIENCE AND REMOTE SENSING. He is the Editor-in-Chief of *Science of Remote Sensing*.

Joshua B. Fisher received the B.S. degree in environmental sciences and the Ph.D. degree in environmental science, policy, and management from the University of California at Berkeley, Berkeley, CA, USA, in 2001 and 2006, respectively.

He did his postdoctoral research at the University of Oxford, Oxford, U.K., and then he joined NASA's Jet Propulsion Laboratory, Pasadena, CA, USA, in 2010. He has focused on ecosystem modeling for over 10 years, developed new models of hydrological and nutrient cycling, and conducted large-scale field campaigns to gather data to parameterize and test models. He is the Science Lead of the ECOSTRESS mission, focused on evapotranspiration. His work bridges modeling and field work, while integrating a wide range of measurement techniques such as eddy covariance and remote sensing.

Yuhu Zhang received the B.S. degree in agronomy from Tarim University, Alaer, China, in 1998, the master's and Ph.D. degrees in geographic information system and physical geography from Xinjiang University, Xinjiang, China, in 2005, and the Ph.D. degree in environmental science from Tsinghua University, Beijing, China, in 2008.

He is an Associate Professor with the College of Resource Environment and Tourism, Capital Normal University, Beijing. His research interests include environmental system analysis, modeling and prediction in climate change and water science, and ecological restoration.

Jie Cheng (Senior Member, IEEE) received the Ph.D. degree in cartography and remote sensing from the Institute of Remote Sensing Applications, Chinese Academy of Sciences, Beijing, China, in 2008.

He was a Post-Doctoral Fellow with the State Key Laboratory of Remote Sensing Science, Beijing Normal University, Beijing, from 2008 to 2010, an Assistant Research Scientist with the University of Maryland, College Park, MD, USA, from 2009 to 2010, and a Visiting Scientist with Hydrology and Remote Sensing Laboratory, U.S. Department of Agriculture, Agricultural Research Service, Beltsville, MD, USA, from 2017 to 2018. He is an Associate Professor with the State Key Laboratory of Remote Sensing Science, Faculty of Geographical Science, Beijing Normal University. His main research interests include estimation of land surface variables from satellite observations, radiative transfer modeling, and studies on surface energy balance.

Jiquan Chen received the B.S. degree in grassland ecology from Inner Mongolia University, Hohhot, China, in 1983, the M.S. degree in forest ecology from the Chinese Academy of Sciences, Beijing, China, in 1986, and the Ph.D. degree in ecosystem analysis from the University of Washington, Seattle, WA, USA, in 1991.

His postdoctoral training was in stream ecology and ecosystem management from 1992 to 1993. He was a Bullard Fellow with Harvard University, Cambridge, MA, USA, from 1999 to 2000. He was a Faculty Member of Michigan Tech University, Houghton, MI, USA, from 1993 to 2001, and also with the University of Toledo, Toledo, OH, USA, from 2001 to 2014. He is currently a Professor with the Department of Geography, Environment, and Spatial Sciences, Michigan State University, East Lansing, MI, USA. His research lies in the coupled effects of global climate change and human activities on terrestrial ecosystems, global change ecology, bioenergy, and carbon/water fluxes. He teaches special topics on coupled human and natural systems, micrometeorological instrumentation and measurements, image processing and GIS, and global change science.

Dr. Chen is a fellow of the AAAS and ESA.

Kun Jia received the B.S. degree in surveying and mapping engineering from Central South University, Changsha, China, in 2006, and the Ph.D. degree in cartography and geographic information system from the Institute of Remote Sensing Applications, Chinese Academy of Sciences, Beijing, China, in 2011.

He is an Associate Professor with the State Key Laboratory of Remote Sensing Science, Faculty of Geographical Science, Beijing Normal University, Beijing. His research interests include the estimation of fractional vegetation cover, land cover classification, and agriculture monitoring using remote sensing data.

Xiaotong Zhang received the Ph.D. degree in cartography and geographical information science from Wuhan University, Wuhan, China, in 2010.

From 2008 to 2010, he was a Joint Ph.D. Student with the Department of Geographical Sciences, University of Maryland, College Park, MD, USA. He is an Associate Professor with the State Key Laboratory of Remote Sensing Science, Faculty of Geographical Science, Beijing Normal University, Beijing. His research interests include the estimation of land surface radiation components from satellite data, and Earth energy balance.

Xiangyi Bei is pursuing the master's degree in cartography and geographical information system with the State Key Laboratory of Remote Sensing Science, Faculty of Geographical Science, Beijing Normal University, Beijing, China.
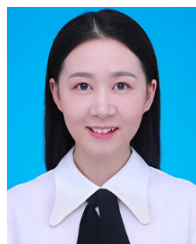
Her research interests include fusion and estimation of terrestrial evapotranspiration by remote sensing.

Ke Shang received the M.S. degree in cartography and geographical information system from Southwest Forestry University, Kunming, China, in 2015. She is pursuing the Ph.D. degree in cartography and geographical information system with the State Key Laboratory of Remote Sensing Science, Faculty of Geographical Science, Beijing Normal University, Beijing, China.

Her research interests include estimation and fusion of terrestrial evapotranspiration using remote sensing data.

Xiaozheng Guo is pursuing the master's degree in cartography and geographical information system with the State Key Laboratory of Remote Sensing Science, Faculty of Geographical Science, Beijing Normal University, Beijing, China.

His research interest is estimating terrestrial latent heat by remote sensing and reanalysis products.

Junming Yang received the M.S. degree from Northeast Agricultural University, Harbin, China, in 2019. He is pursuing the Ph.D. degree in cartography and geographical information system with the State Key Laboratory of Remote Sensing Science, Faculty of Geographical Science, Beijing Normal University, Beijing, China.

His research interest focuses on multisource remote sensing data fusion and its application in agriculture soil and water resources.